JMEPEG
https://doi.org/10.1007/s11665-023-08671-1

1059-9495/$19.00

ORIGINAL RESEARCH ARTICLE

Temperature Evolution, Material Flow, and Resulting Mechanical Properties as a Function of Tool Geometry during Friction Stir Welding of AA6082

Aleksandra Laska, Behzad Sadeghi, Behzad Sadeghian, Aboozar Taherizadeh, Marek Szkodo, and Pasquale Cavaliere

Submitted: 18 April 2023 / Revised: 11 August 2023 / Accepted: 18 August 2023

The friction stir welding process was simulated for joining AA6082 aluminum alloy with the use of the computational fluid dynamics method. Two different tool geometries were used—a tapered cylindrical pin (simple pin) and a hexagonal pin with grooves (complex pin). The analysis of the simulations performed was discussed in terms of temperature evolution during the process, total heat input, residual stresses and material flow. Simulations revealed that a 5% higher temperature, equal to maximum 406 °C, was provided when using the complex pin than with the simple pin. Higher temperature and higher shear stresses during the welding with the complex pin caused the introduction of higher residual stresses in the weld. Experimental results on the produced welds allowed observation of the microstructure of the joints, hardness tests in cross sections and tensile strength tests. Due to the higher temperature during the process with the complex pin and the more efficient recrystallization process, grain refinement in the SZ was more pronounced. The average grain size in the stir zone for the weld produced with the complex pin was equal to 11 $\pm$ 1 μm, and in the case of the simple pin 14 $\pm$ 1 μm. The presented hardness profiles revealed that the weld produced with a complex pin had higher hardness in the stir zone, equal to 89.5 $\pm$ 1.3 HV, which is consistent with the Hall-Petch relationship. The obtained UTS values corresponded to the joint efficiency of 72.5 $\pm$ 4.9% and 55.8 $\pm$ 8.6% for the weld produced with the complex pin and the simple pin.

Keywords aluminum alloys, computational fluid dynamics, COMSOL, friction stir welding, mechanical properties, microstructure

1. Introduction

Friction Stir Welding (FSW) is a method gaining increasing interest, especially for joining light metals such as aluminum and its alloys. Patented in 1991, the method is based on joining materials by plasticizing and mixing them in the weld zone by using a non-consumable tool (Ref 1, 2). The tool consists of two integral parts–a pin and a shoulder. During the process, the tool performs both rotational and traverse motions. The tool shoulder is in constant contact with the surface of the components in contact with each other. The friction generated by the movement of the tool is transformed into heat, which leads to the plasticization of the material (Ref 3). At the same time, the pin performing rotational motion mixes the material, and the tool moves in a traverse motion along the weld line (Ref 4). The most important process parameters include the tool's tilt angle, traverse and rotational speed, as well as the geometry of the tool (Ref 5). Properly selected process parameters, by ensuring optimum temperature and proper mixing of the weld material, allow to obtain sound joints characterized by low residual stresses, high mechanical and electrochemical properties (Ref 6, 7).

Among the greatest advantages of the FSW method is the ability to join materials presenting low weldability (Ref 8). Such materials include aluminum alloys from all groups, including the 6xxx group. Due to their properties such as low density, relatively high strength and corrosion resistance, as well as its low price, it is a good competitor to steel for, for example, train car structures (Ref 9). Among other alloys of 6xxx series, AA6082 alloy is a popular choice for several applications due to its superior properties, high strength, durability, and excellent corrosion resistance. However, problems in joining aluminum require the development of a method of successive joining of this alloy (Ref 10). An excellent solution is the FSW method. The main problems arising from the welding of aluminum alloys by conventional methods are their extreme susceptibility to solidification cracking and porosity associated with the change in state (Ref 11, 12). Therefore, using a solid-state joining process such as FSW eliminates this problem.

Due to the complexity of the mixing process during the welding, the limitations of the equipment, and possible uncertainties due to the experimental procedures, advanced investigations of the thermal process by the real experiments are still challenging. The combination of temperature changes and effective weld strain can play a constant role in determining

Aleksandra Laska and **Marek Szkodo**, Faculty of Mechanical Engineering and Ship Technology, Gdansk University of Technology, Narutowicza 11/12, 80-233 Gdańsk, Poland; **Behzad Sadeghi** and **Pasquale Cavaliere**, Department of Innovation Engineering, University of Salento, Via per Arnesano, 73100 Lecce, Italy; and **Behzad Sadeghian** and **Aboozar Taherizadeh**, Department of Materials Engineering, Isfahan University of Technology, Isfahan 8415683111, Iran. Contact e-mail: aleksandra.laska@pg.edu.pl.

Published online: 31 August 2023

the grain size and distribution of precipitates, and consequently the mechanical properties of the sample after the welding process (Ref 13). In addition, conducting actual experiments involves a considerable financial effort, and therefore present trends are shifting toward computer simulations. Due to the difficulty and time-consuming nature of experimentally measuring grain size, residual stresses, type and size of precipitates and thermal history in the joint area, the finite element method (FEM) is justified (Ref 14). On the contrary, numerical modeling of FSW is a demanding process actually, mainly due to material assumptions and boundary conditions.

In order to analyze the temperature history, material movement, distortion, strain rates, recrystallization and residual stresses evolution, thermal-mechanical models are widely applied to simulate the FSW process. Among them, the models such as Coupled Eulerian–Lagrangian (CEL) model, Computational Fluid Dynamics (CFD) model, arbitrary Lagrangian (AL), and arbitrary Lagrangian–Eulerian (ALE) can be distinguished (Ref 15, 16). One of the most widely adopted approaches of the numerical simulations of the FSW is computational fluid dynamics (CFD). Seidel and Reynolds (Ref 17) presented a two-dimensional model coupled with a thermal model. This model was created by assuming laminar, viscous and non-Newtonian flow around the pin. They showed that the transport of material mainly occurs in retreat side. Bendzsak et al. (Ref 18), in practical research, obtained the viscosity of aluminum alloy as a function of strain rate and temperature. Ulysse (Ref 19) obtained the influence of speed parameters on temperature and forces during FSW by constructing a three-dimensional viscoplastic model. Colegrove et al. (Ref 20, 21) studied the temperature distribution and material flow during welding of aluminum alloys by developing 3D numerical simulations with the CFD approach by the use different tool geometries–smooth and threaded tool. Nandan et al. (Ref 22-24) analyzed the heat transfer, plastic flow and the effect of material flow rates during FSW for aluminum alloy, stainless steel and mild steel. In these researches they considered the non-Newtonian viscosity as a function of temperature and strain rate. Kim et al. (Ref 25), using the finite volume method (FVM), investigated the temperature distribution and material flow during friction stir welding of 5083 aluminum alloy. They showed that the CFD method is more effective than other proposed methods such as ALE, although it cannot investigate the phenomenon of material hardening (Ref 26). Hasan et al. (Ref 27) applied a CFD model to predict tool wear during the FSW of AISI 304 austenitic stainless steel. The influence of tool geometry in the FSW process has been widely analyzed by conducting computer simulations, especially CFD method, by Ji et al. (Ref 28), Zhang et al. (Ref 29), Hirasawa et al. (Ref 30) and Yu et al. (Ref 31). However, the current state-of-the-art is deficient in analyzing the effect of tool geometry on the properties of AA6082 aluminum alloy welds. In addition, the original tool geometries analyzed in this study, to the best of the authors' knowledge, have not yet been analyzed for friction stir welded AA6082 alloy.

The following work analyzes the effect of tool geometry on the properties of AA6082 joints produced by the FSW process. Based on computer simulations performed, the contributions of temperature, total heat input, residual stresses and material flow were discussed. In addition, the effects of these factors on the microstructure, hardness and tensile strength of the resulting welds were determined through performed experiments.

2. Experimental Procedure

2.1 FSW Procedure

The material used in this study was AA6082 aluminum alloy, solution heat-treated and artificially aged to T651 condition. The rolled sheets of 3 mm in thickness were used to perform Friction Stir Welding process.

The welding process was conducted on a conventional milling machine (FU251, Friedrich Engels Kazanluk, Bulgaria). To establish the influence of the tool geometry on the properties of resulting welds, two different tools were chosen. The shoulder geometry was in both cases identical. The two tools differed in the shape and dimensions of the pins. The exact geometries of the tools with the tapered cylindrical pin and the hexagonal pin with grooves are presented in Fig. 1. The material of the pins was 73MoV52 tool steel and the shoulder was made of X210Cr12 tool steel. The hardness values of the pin and the shoulder were equal to 58 and 61 HRC, respectively (Wilson Mechanical Instrument Co. Inc., USA). The employed tool traverse speed was 250 mm/min, the tool rotational speed was 1000 rpm and the tool tilt angle was 2°. The proposed welding parameters were based on previous experience with the friction stir welding of AA6082 alloy (Ref 32).

2.2 Modeling

In this research, a finite element model was used to simulate the heat generation, material flow, and residual thermal stress during friction stir welding (FSW). In the following paragraphs, the equations for obtaining heat generated in the FSW process are presented. It should be noted that the detailed description of the parameters is provided in the references (Ref 22, 33, 34) (Fig. 2).

In this model the temperature distribution model was considered based on the steady state heat transfer equation, considering the translational motion, according to Eq 1 (Ref 23, 35).

$$\rho C_{\mathrm{p}} U(\nabla T) = \nabla(k \nabla T) + \dot{Q} \qquad \text{(Eq 1)}$$

The heat generated in the cylindrical part of the pin was calculated using Eq 2. The heat generated in the hexagonal part of the pin was calculated using Eq 3. These equations are based on the work of Waheed et al. (Ref 36). The tangential velocity of each point of the tool on the workpiece and also the heat generated under the shoulder was obtained according to Darvazi et al.'s work (Ref 33).

$$Q_{\mathrm{pin\_Circle}} = \int_0^{2\pi} \int_0^{R_{\mathrm{C}}} \mu p r(\omega r - U\psi \sin(\theta)) \mathrm{d}r\mathrm{d}\theta \qquad \text{(Eq 2)}$$

$$Q_{\mathrm{pin\_Hexagon}} = \int_0^{2\pi} int_0^{R_{\mathrm{H}}} \mu p r(\omega r - U\psi \sin(\theta)) \mathrm{d}r\mathrm{d}\theta - \int_0^{\frac{\pi}{6}} \int_0^{R_{\mathrm{H}}} \mu p r(\omega r - U\psi \sin(\theta)) \mathrm{d}r\mathrm{d}\theta \qquad \text{(Eq 3)}$$

The heat generated was divided into two general parts: heat produced by friction and heat produced by plastic deformation. The total heat generated was calculated using Eq 4. This equation takes into account the effect of sliding and sticking friction, as well as the effect of heat generated by plastic deformation during welding.

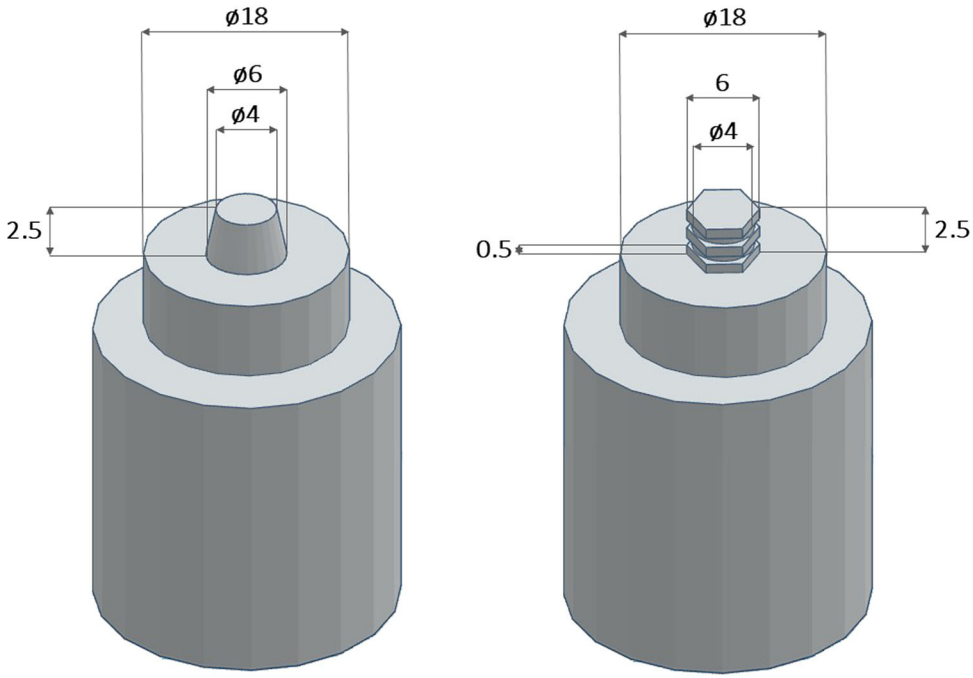

Fig. 1 Schematic illustration of the geometry of the tool used for FSW of AA6082

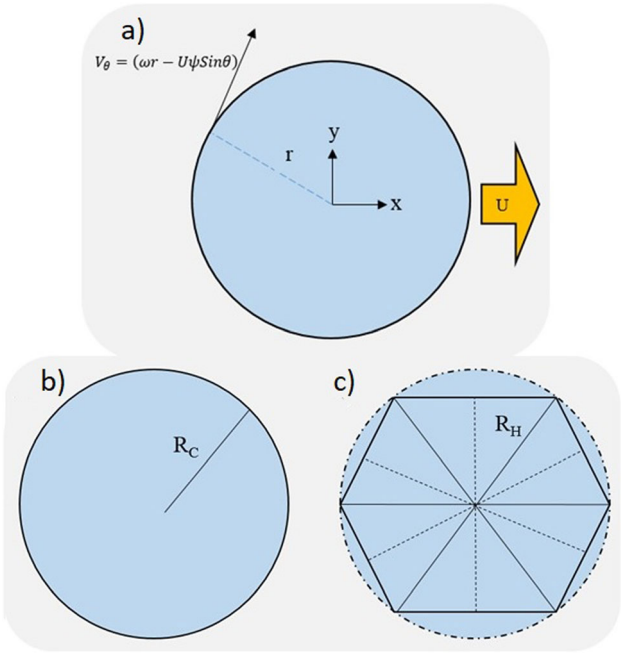

Fig. 2 Schematic of tangential velocity model during FSW process (a), schematic of a circular pin (b) and a hexagonal pin (c) sections

$$F = (1 - S)\tau\eta + S(\delta\tau\eta + (1 - \delta)\mu P_N) \quad \text{(Eq 4)}$$

Computational fluid dynamics (CFD) was applied to model the material flow during FSW process. To this purpose, the continuity and Navier-Stokes equations for single phase material were used according to Eq. 5 and 6 (Ref 37, 38). The parameters of these equations including the dynamic viscosity, and strain rate, which were obtained from other references (Ref 24, 37, 38).

$$\nabla . U = 0 \quad \text{(Eq 5)}$$

$$\rho U . \nabla U = -\nabla p + \mu \nabla^2 U \quad \text{(Eq 6)}$$

In order to predict the residual thermal stress, a thermo-mechanical model was used. The total strain and thermal strain were calculated according to Eq. 7 and 8 (Ref 39)

$$\varepsilon = \varepsilon^M + \varepsilon^T \quad \text{(Eq 7)}$$

$$\varepsilon^T = \alpha \Delta T \quad \text{(Eq 8)}$$

The finite element model was created using COMSOL Multiphysics version 5.3 software. In this model, triangular elements were created automatically on the surfaces of the geometry. The element size ranged from 0.05 to 5 mm, and the elements on the bottom surface of the tool were much smaller than other free surfaces. Total number of triangular elements was 12868 and number of edge elements was 992.

The model boundary conditions were applied using coupled thermal-CFD and thermal-mechanical analysis. The boundary conditions used in the thermal solution in this model included the convective heat transfer from the upper surface and side surfaces and the conductive heat transfer from the lower surface assuming an iron substrate. Radiant heat transfer boundary condition was considered for all surfaces. The boundary condition used in the CFD solution was using a sliding surface considering circular motion forces in the area under the tool. Also, in the thermal-mechanical solution, the side surfaces of the part were considered as fixed surfaces.

2.3 Materials Characterization

After the welding process, the samples were cut in order to perform microstructure investigation, tensile and hardness tests. In order to perform the microstructure observations on the cross

sections, the specimens were cut in the size of 300 × 10 mm. The samples were wet ground to the final gradation of #4000 and polished with a 1 μm diamond suspension. A double-stage etching was performed using Weck's etchant. Firstly, the metallographic samples were etched in a 2 wt.% NaOH solution for 60 s. Then, the samples were immersed for 10 s in a solution of 4 g KMnO4, 1 g NaOH and 100 mL of distilled water. The microstructural observations were performed using an optical microscope (BX51, OLYMPUS, Japan), in accordance with the ASTM E3 standard-Standard Guide for Preparation of Metallographic Specimens. The average grain size was calculated with the use of the linear intercept method, according to ASTM E112-13 standard-Standard Test Methods for Determining Average Grain Size.

The microhardness distributions measurements were performed on the cross sections of the produced joints at the distance of 1.5 mm from the weld face. A Vickers microhardness tester (Future-Tech FM-800, Tokyo, Japan) with the load of 1 N was used.

The tensile properties of the produced welds were performed with a universal testing machine (Zwick/Roell 100, Germany). Three samples were tested in order to calculate their standard deviation. The geometry of the tensile sample is presented in Fig. 3. The fracture surfaces of the samples after the tensile tests were investigated by a high-resolution scanning electron microscope (SEM) (Phenom XL, Thermo Fisher Scientific, The Netherlands) with a backscattered electron detector (BSE).

3. Results and Discussion

Figure 4(a) and (b) shows the three-dimensional and two-dimensional contour plot of the simulated temperature distribution during the FSW process with the hexagonal pin with grooves (complex pin). It can be seen that in the AS region, the temperature is higher than in the RS region. The thermal results are in good agreement with the model obtained from previous researches. The simulation results show that this model could be used to predict temperature profiles for other simulations. In addition, it can be seen that there is a clear asymmetry in the welding section, which indicates the existence of AS and RS regions.

It can be seen that the maximum temperature is below the tool. This is because the material in the top surface of the workpiece move parallel to the shoulder of the tool and therefore has a higher shear rate and more heat is generated. This result is in consistent with the results obtained in previous researches (Ref 23, 33, 37, 40, 41). On the other hand, the heat-affected zone (HAZ) is larger on the AS side. It can also be seen that the temperature around the pin and under the shoulder is higher, which indicates the heat-generating areas.

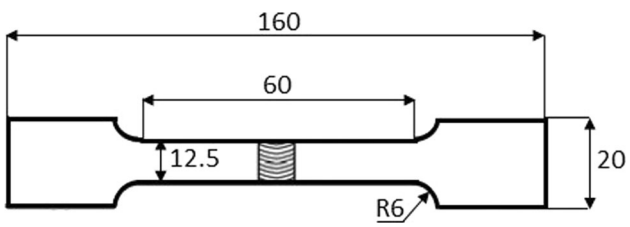

Fig. 3 Geometry of a tensile sample

By observing Fig. 4(a) and (b), it can be seen that the temperature gradient is clearly higher in front of the tool than behind the tool. This phenomenon is mainly caused by the different heat transfer properties of the cool zone and the heated zone. Therefore, it is easy to conclude that the heat is transferred at a higher rate to the front and at a lower rate to the back of the tool.

Figure 4(c) and (d) shows the results of the thermal simulation of the FSW process of aluminum alloy 6082, with the tapered cylindrical pin (simple pin) and with the same welding conditions as before, in a 2D section and a 3D plot. By comparing the results of the simple pin and the previous state (complex pin), it can be seen that the maximum temperature produced by the complex pin is at least 5% higher. The reason for this is the presence of more shear stresses in the corners of the pin and the presence of more heat producing surfaces in this pin model.

By observing the three-dimensional plot of the heat generated by the pin, according to Fig. 5(a), it can be seen that the heat generated (W/m^2) around the hexagonal region is higher than in the cylindrical region. The reason for this is in the geometric form and the compliance of the heat generated according to the equations mentioned in the previous section. In fact, the presence of many corners in the geometry of the hexagonal pin leads to higher shear stress and, therefore, higher heat generation. Additionally, the area of this zone is also effective on the heat generation in this solution. By comparing the results obtained from the heat generated around the simple pin, in comparison with the complex pin, according to Fig. 5(b), it can be seen that the heat generated by the complex pin is at least 20% higher than the simple pin, which is due to the presence of sharp corners of the complex pin. Therefore, this causes more heat generation due to shear stress in the specimen.

By using the results of temperature distribution and by performing the simulation in the transient state solution, based on the obtained results from steady state solution, the thermal residual stress distribution in the parts was obtained. Fig. 5(c) shows the distribution of residual thermal stress in the cross section of the weld produced with the complex pin. It should be noted that the obtained graph is in good agreement with previous researches (Ref 34, 35, 42, 43). Since the residual thermal stresses are the result of thermal expansion and contraction of the material, by comparing the thermal results and the residual stress simulation results, it can be seen that due to the presence of a region with a maximum temperature in the middle line of welding, the stress in this region is higher and of course it is tensile. In the far areas and around the edge of the workpiece, the stress is compressive.

By comparing the thermal residual stress obtained from the FSW process with the complex pin in comparison with the simple pin, as shown in Fig. 5(d), it can be seen that the residual stress in the case of the simple pin is at least 13% lower than the complex case. The reason for this, as mentioned earlier, is the higher average temperature around the complex pin, due to higher shear stress than the simple pin. This causes the higher maximum temperature in the center line of the weld in the complex pin compared to the simple pin, and therefore the thermal residual stress increases.

Figure 6(a) and (b) shows the CFD simulation results, material flow velocity, of the FSW process. It can be seen that the maximum velocity of material flow is in the area below the surface of the tool shoulder. The reason for this is the higher

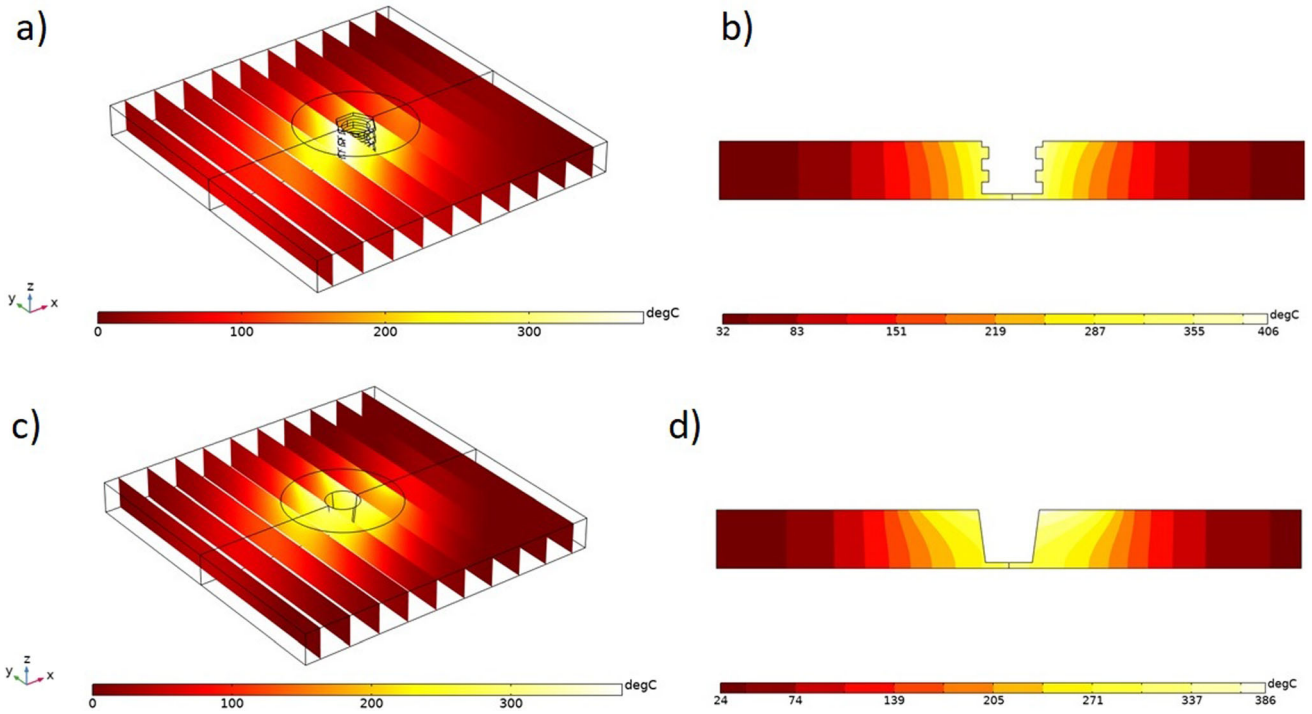

Fig. 4 3D (a) and 2D (b) plot of temperature distribution during FSW for a hexagonal pin and 3D (c) and 2D (d) plot of temperature distribution during FSW for a circular pin

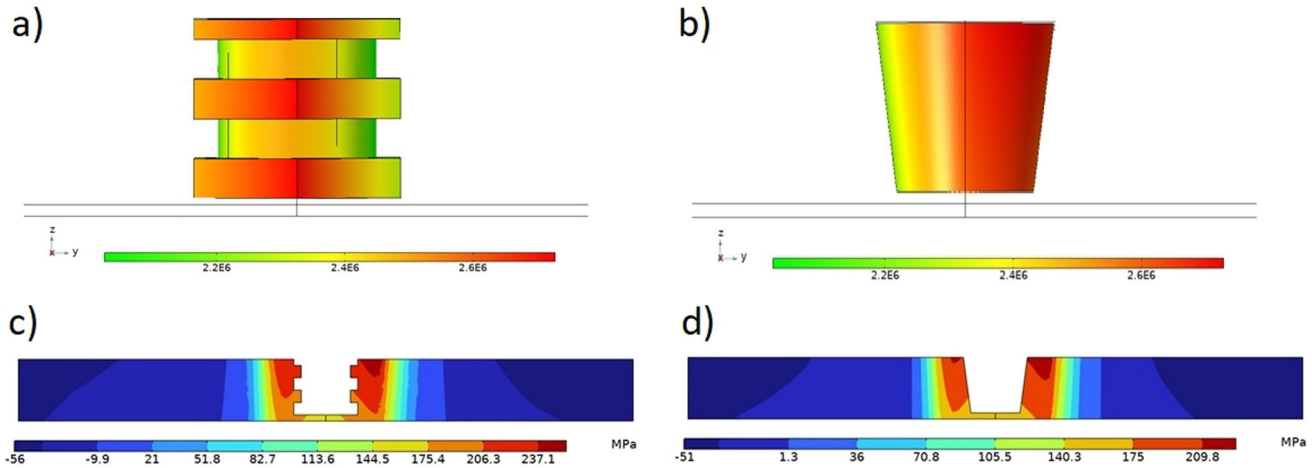

Fig. 5 Simulated heat generated plot on a complex pin (a) and a simple pin (b), and residual thermals stresses in the cross section of the specimen during FSW with a complex pin (c) and a simple pin (d)

temperature under the surface of the tool and the application of more shear stress from the tool in this area. High shear stress and temperature by softening the material and reducing the dynamic viscosity lead to the flow of the material in the direction of tool rotation. Especially in aluminum alloy, which properties are highly dependent on temperature and strain rate.

Figure 6(c) and (d) shows the velocity of material flow and stream lines around the pin in two circular and hexagonal regions, both in the case of the hexagonal pin. As can be seen, the maximum velocity of the material flow around the hexagonal region is at least 40% higher than the circular one. The reason for this is the higher heat generated around the hexagonal area and also due to the higher shear stresses around the tool in this area, therefore, the dynamic viscosity of the material decreases and as a result, the flow rate increases.

It can be seen that there are flow separations around the hexagonal pin, which took on the hexagonal zone. The reason for these separations is the presence of deformation zones in the pin. These regions are less visible around the circular pin, however, around the circular pin in the RS region there are signs of flow separation, which, due to their polygonal shape, are caused by the flow created by the hexagonal pin at the top and bottom of this area.

By observing the stream lines, it can be seen that the lines around the edges parallel to the shoulder of the tool have more accumulation, this is actually the thermo-mechanically affected zone (TMAZ). In fact, the thermo-mechanical work is more due

to the high temperature and strain rate in these areas. On the other hand, around the hexagonal pin, the stream lines have more density than in the circular area, which is because of the existence of shear stresses around the hexagonal pin.

By comparing the results of the material flow during the FSW process in the simple pin compared to the complex pin, according to Fig. 7(a) and (b), it can be seen that the velocity of the material around the pin and under the shoulder of the tool is almost equal. In case of complex pin, according to Fig. 6(b), the flow velocity under the tool is much higher than around the pin. The reason for this is that the flow of the material is wrapped around the pin at different levels of the tool, but in a simple pin, due to the slope, the material finds a simpler flow around the pin, so it has a higher velocity.

This issue is clearly seen in Fig. 7(c), as it can be seen that around the simple pin, in a section, the velocity of the material

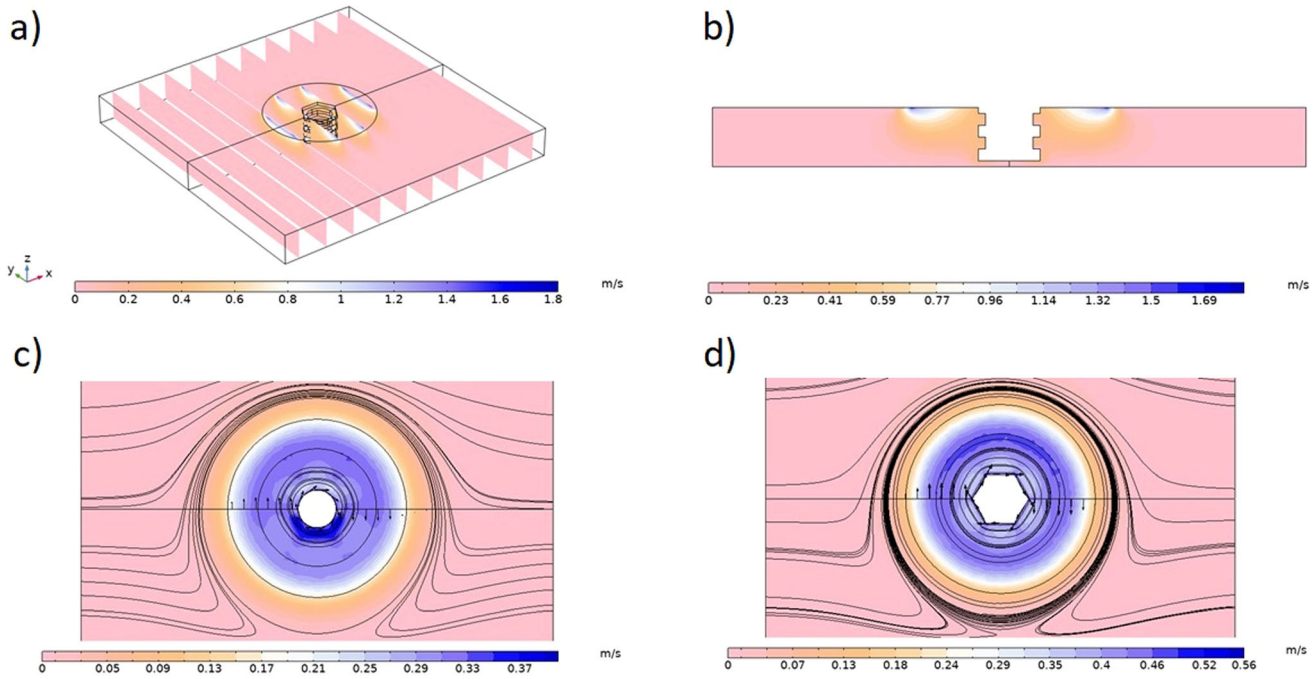

Fig. 6 3D (a) and 2D (b) plot of material flow velocity for a complex pin and 2D contour plot in the cross sections around the circular (c) and hexagonal (d) zone of the pin

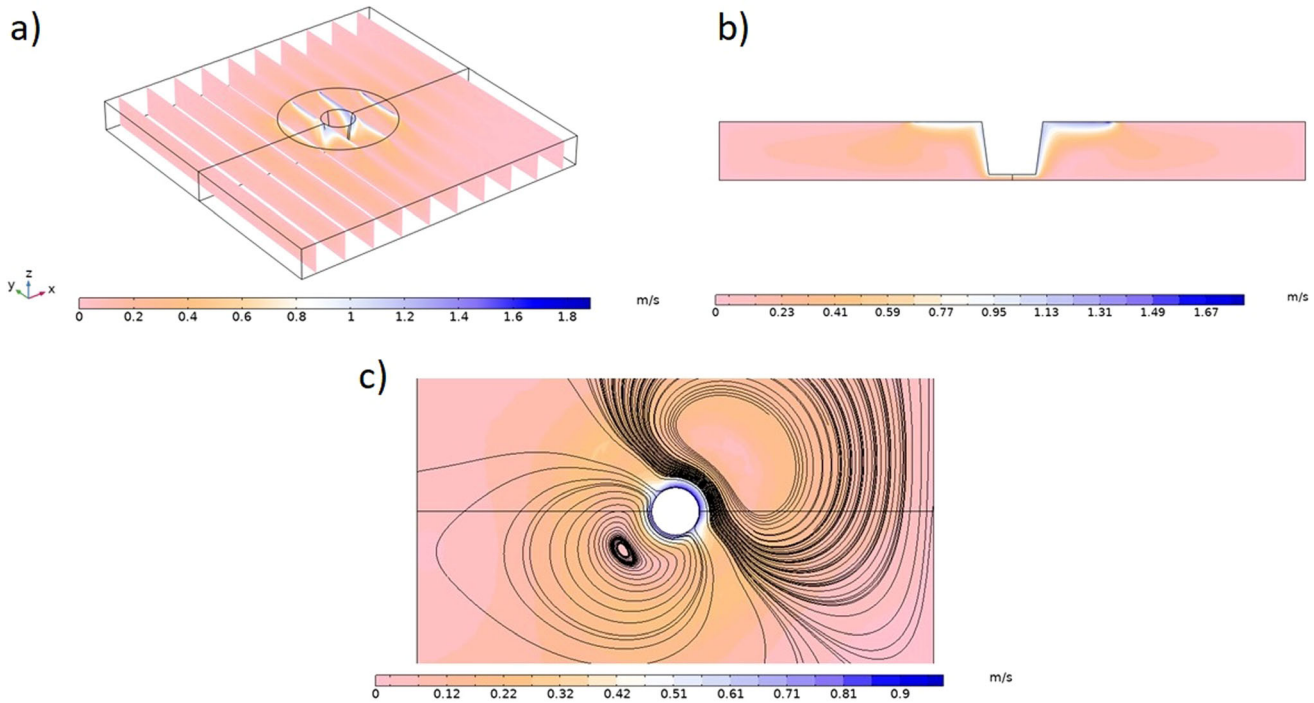

Fig. 7 3D (a) and 2D (b) plot of material flow velocity for a simple pin and 2D contour plot in the cross sections around the simple pin (c)

flow is very high, but in the distant areas, this speed is low. In comparison with Fig. 5(c) and (d), which is related to the complex pin, it can be seen that, whether in the circular region or the hexagonal, the fluidity of the material around the pin is low and it is more in the distant regions. In fact, the presence of a slope in a simple pin causes more flow and the material has a higher flow around the pin. But the presence of different levels for material flow in the complex pin leads to the trapping of the material in one area and the flow around the pin is reduced. Therefore, due to the high shear rate generated by the shoulder of the tool, the velocity of the material increases in the distant areas.

Obviously, the thermomechanical behavior of the material during FSW strongly influences the final microstructural properties and mechanical performances of the welds.

Visual inspections were performed to determine the quality of the produced welds. Figure 8 presents the images of the weld seam surfaces. In the produced welds, no serious defects like grooves or lacks of bonding were observed. Also, no material outflow was found. In the case of the sample produced with a tapered cylindrical pin (Fig. 8a) some cavitation loses can be observed. It might be caused by insufficient plasticization of the material due to the lower heat input in the case of the simple pin. The performed computer simulations revealed that by applying the hexagonal pin with grooves, the amount of heat generated during the process is around 20% higher, when compared to the process with the use of tapered cylindrical pin (see Fig. 5a and b). This is due to the presence of sharp corners of the complex pin, and it causes more heat generation due to shear stress in the specimen. It is claimed that the key factors determining the quality of the weld are adequate heat input and proper stirring of the plasticized material. Therefore, for the weld produced with the hexagonal pin, higher heat input and better plasticization and mixing of the material resulted in the formation of a non-defective weld seam.

In order to define the influence of the tool geometry on the grain structure of the joints, the macro- and microstructural observations were performed. Fig. 9 presents the macrostructure of the resulting welds, and Fig. 10 illustrates the microstructure of the welds in different zones.

Based on the micro- and macrostructure observations it can be concluded that the geometry of the tool strongly influences the macrostructure of the weld. High temperatures, large deformations, strains, strain rate and the total heat input are the factors strongly dependent on the process parameters, including the tool geometry. In the case of the weld produced with the tapered cylindrical pin, the width of the stir zone (SZ) is larger. The width of the SZ measured in the center line of the cross section was equal to 8.25 mm for the tapered cylindrical pin, and 6.80 mm in the case of the hexagonal pin with grooves. Despite the temperature being about 5% higher when using a complex pin compared to a straight pin and the greater total heat input, the mixing process differed between the two cases. CFD simulation results showed that mixing the plasticized material through the complex pin leads to the trapping of the material in some areas and the flow around the pin is reduced. With a simple pin, due to the slope, the material finds a simpler flow around the pin, so it has a higher velocity, which results in the wider stir zone area. However, higher temperature during the process with the complex pin and the larger total heat input resulted in a wider heat-affected zone (HAZ) comparing the weld produced with the simple pin. It should also be noted that the zone directly under the shoulder is of similar width in both cases, reflecting the geometry of the tool. Simulation results indicated that the material mixing velocity is the highest in this region. This is attributed to higher temperature below the tool surface and higher shear stress applied from the tool. High shear stress and temperature by softening the material and reducing dynamic viscosity lead to the increased flow of the material in the direction of tool rotation. Therefore, the micro- and macrostructure of the upper weld zone is primarily related to the impact of the tool shoulder during the process, rather than the pin itself.

Discussing the obtained pictures it can be noted that no internal defects typical of the FSW process were found. The asymmetries of the weld cross sections can be clearly observed, indicating the advancing and retreating sides of the welds. The differences mainly relate to the size of the different zones, which is particularly evident in the HAZ. On the AS side, it is larger, which agrees with the results of the simulations performed (Fig. 4b and d). Typically for a FSW joint, the weld nugget zone consists of a fine-grained structure formed by the recrystallization process in the stir zone (SZ), thermo-mechanically affected zone (TMAZ) and heat-affected zone

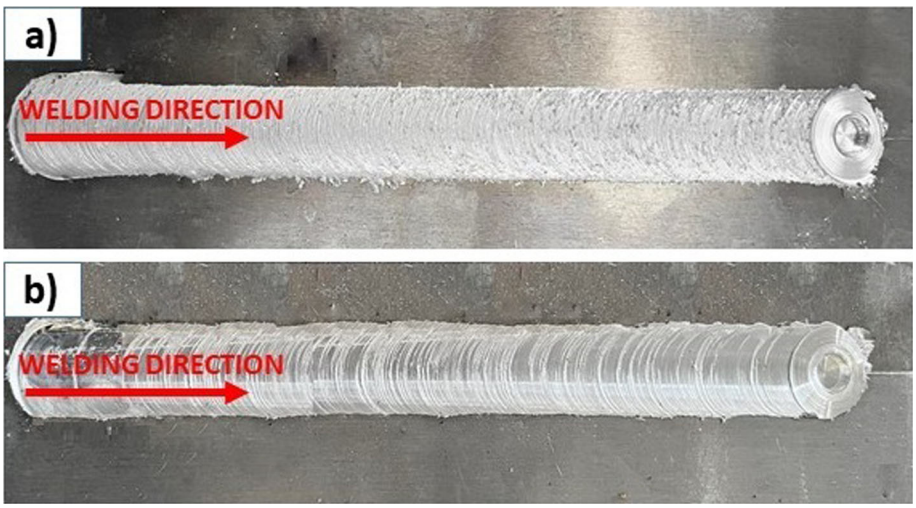

Fig. 8 Friction stir welded samples produced with the tapered cylindrical pin (a) and the hexagonal pin with grooves (b)

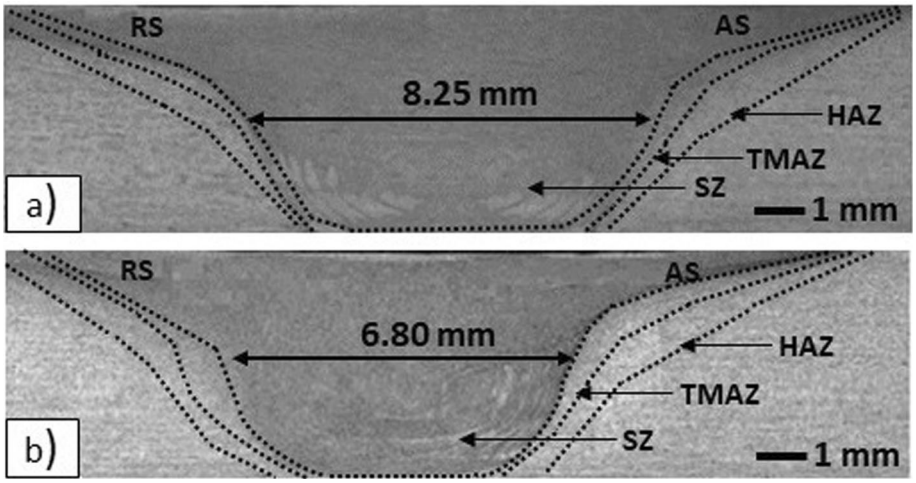

Fig. 9 Macrostructure of the welds produced with the tapered cylindrical pin (a) and the hexagonal pin with grooves (b)

(HAZ). It is obvious that the grain size reduces from HAZ to SZ for both AS and RS, which agrees with the previous studies on friction stir welded aluminum alloys (Ref 44, 45). In the case of a complex tool, finer grains can be observed in the SZ. Computer simulations demonstrated that during the FSW process using a hexagonal pin with grooves, the maximum temperature in the stirring zone is at least 5% higher compared to a tapered cylindrical pin. Due to the higher heat input, the recrystallization process occurred more efficiently, resulting in a finer-grained microstructure. The average grain size in the SZ of the weld produced with the simple pin was equal to 14 ± 1 μm, and for the weld produced with the complex pin 11 ± 1 μm. According to the Hall-Petch relationship, smaller grain size affect the increase of the hardness of the material (Ref 46, 47). Higher heat input during the FSW process results in greater grain refinement due to more efficient recrystallization, which enhances the strength of the SZ.

The microhardness profiles of the joints produced with the hexagonal pin with grooves and the tapered cylindrical pin tool are presented in Fig. 11.

The microhardness of the base metal AA6082 was established as 96 ± 3.9 HV. It should be noted that the reduction of the microhardness in the entire joint's cross section can be observed. The highest reduction in the microhardness in both cases can be observed in the heat-affected zones. The lowest values of approximately 62 and 67 HV can be observed on the advancing side of the welds produced with the simple and complex pin, respectively. More significant decrease in hardness in the heat-affected zone on the advancing side is consistent with the results of the simulations performed, where greater heat input was observed on the advancing side for the process involving both tools (Fig. 4a and b). In precipitation strengthened aluminum alloys the evolution of microstructure upon heating, plastic deformation and further cooling that occur in the stir zone is very complex. The coherent strengthening phase is dissolved as a result of severe deformation and an increase of temperature. In precipitation hardened alloys such as AA6082, during the FSW process, heating the material well above the dissolution temperature of the initial precipitates enables dissolution, reprecipitation and overaging. In precipitation hardened alloys it is widely accepted that some coarsening of precipitates is occurring, and possible dissolution at higher temperatures (Ref 48). It should be emphasized that in the heat-treatable alloys, factors such as grain size and dislocation density also affect strength, and the simultaneous effects of changes in precipitation hardening make determining the influence of individual factors an elaborate issue. Heat-treated aluminum alloys derive much of the strength from the existence of fine precipitates created during previous heat treatment (precipitation hardening). Thermal cycles occurring during welding can lead to precipitates coarsening or dissolving and further precipitation during or after cooling. In the HAZ, softening is observed, with a rapid drop in hardness as the TMAZ is approached. As the temperature in the HAZ increases, the process of dissolution of precipitates is intensified, leading to the decrease in strength in this zone. The heat input in the welding process is a crucial factor, as it causes the overaging of the strengthening phase and grain growth. For precipitation-strengthening alloys, such as AA6082, dissolution or coarsening of precipitates lead to drastic reduction in the hardness. The normal hardening precipitate in AA6082 is β'' (Mg_5Si_6), but this can dissolve easily at temperatures of 200-250 °C, which are easily reached in the HAZ. Another precipitate, β' ($Mg_{1.7}Si$), forms on dispersoids in the matrix very easily at 300 °C (Ref 49). Based on the conducted simulations, by analyzing temperature distribution during the process (Fig. 4b and d) it is evident that such temperatures were achieved in HAZ during welding. It should be also noted that the HAZ of HAZ/TMAZ interface is often the location of the failure during tensile tests (Ref 50-52). The results of the simulations clearly indicated the asymmetry of the process and the existence of advancing and retreating sides. Also, the microhardness profile confirms this theory, where different hardness values are observed in different zones on both sides of the weld, as well as their different sizes. The results of simulations indicated that the larger size of the HAZ is observed of the advancing side (Fig. 4b and d), which is also noticeable on the microhardness profiles, especially in the case of the weld produced with the complex pin. Also in this case, the location of the HAZ is closer to the weld center, which indicates a smaller size of the stir zone. These observations are in a good agreement with the macrostructural observations (Fig. 9). The greatest recovery in strength is observed in the nugget. Both coarsening and dissolution lead to a drop in hardness, but strength recovery only occurs following dissolution. In the case of the weld produced with a simple tool, the

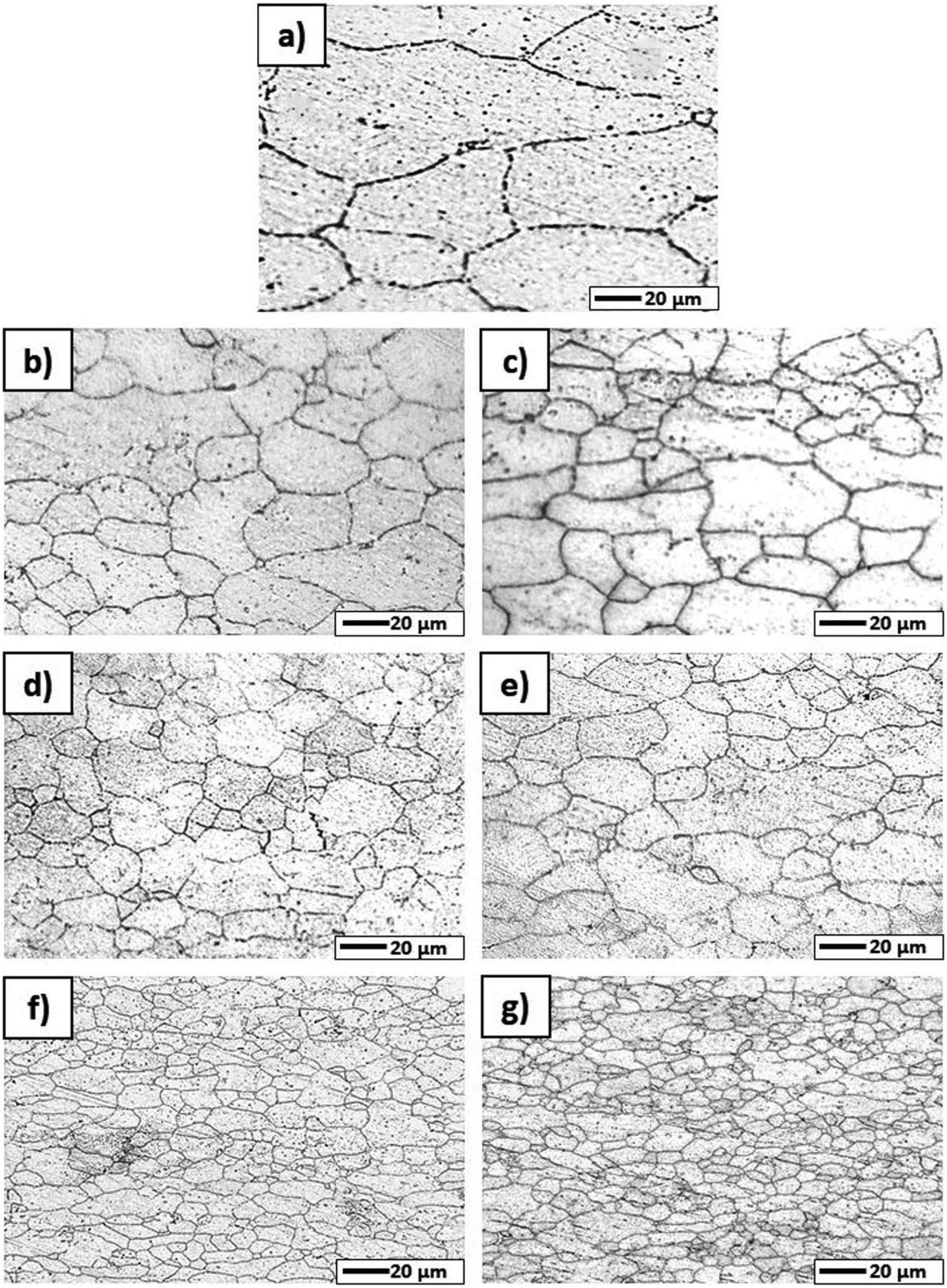

Fig. 10 Microstructure of the base material AA6082 (a) and welds produced with the tapered cylindrical pin in the HAZ (b), TMAZ (d) and SZ (f) and the hexagonal pin with grooves in the HAZ (c), TMAZ (e) and SZ (g)

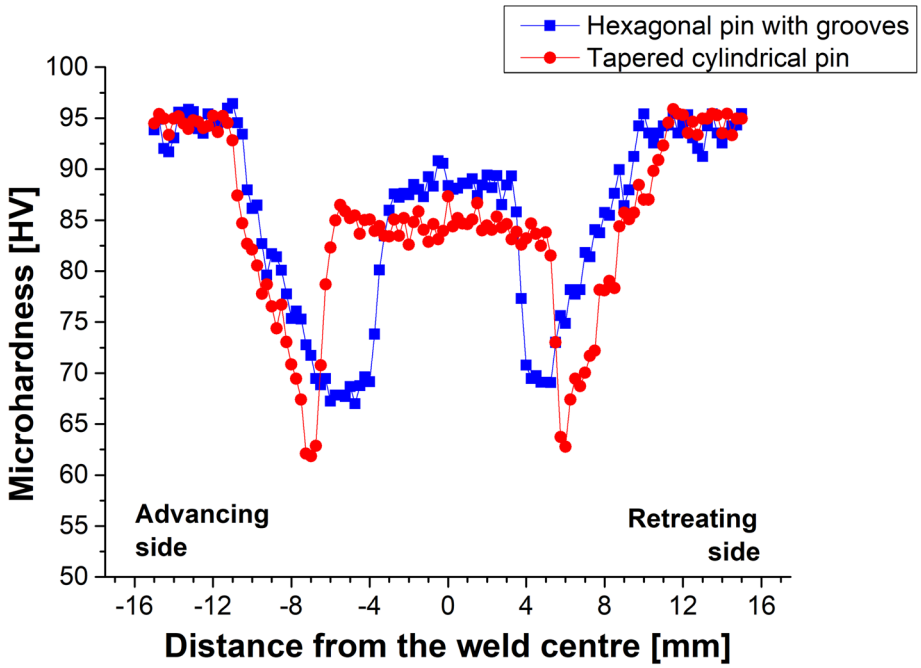

Fig. 11 Microhardness profiled of the FSW joints produced with different tools at the distance of 1.5 mm from the weld face

nugget zone is larger, which was also proved by macroscopic imaging (Fig. 9). The maximum hardness in the nugget zone of the joint produced with a simple pin is equal to 84.5 ± 1.9 HV and it is lower comparing to the hardness of the nugget zone of a weld produced with a complex tool, where the measured hardness was equal to 89.5 ± 1.3 HV. In the nugget zone of the weld produced with the complex tool, the geometry of the hexagonal pin lead to higher shear stress, and therefore, higher heat generation. The conducted simulations revealed that the maximum temperature in the stir zone of the weld produced with complex pin is 5% higher than in the case of the simple pin. It leads to more effective recrystallization process. Microscopic observations allowed to observe lower grain size in the nugget zone of the weld produced with the complex pin. The reduction in the grain size leads to the increase in the hardness, according to the Hall-Petch relationship (Ref 46, 47, 53). Also, this geometry of the tool promotes better plasticizing and mixing of the material in the nugget zone, leading to more uniform microstructure and reducing the risk of defects resulting from improper mixing of the material.

The produced joints, as well as the base metal were tensile tested on the universal testing machine. Fig. 12 presents the failure locations of the welded samples after tensile tests. Fig. 13 illustrates stress-strain curves for the investigated welds and the base material AA6082 (a) and their average ultimate tensile strength (UTS) values (b). The joint efficiency values were calculated. Joint efficiency refers to the strength of a welded joints with respect to the strength of the base metal AA6082.

The highest value of UTS was found for AA6082 base material equal to 371 ± 21 MPa. In case of the welds, the values of 269 ± 18 and 207 ± 32 MPa were noted for the joints produced with hexagonal pin with grooves and tapered cylindrical pin, respectively. It corresponds to the joint efficiency of 72.5 ± 4.9 and 55.8 ± 8.6 %. In both of the cases, the location of the failure was detected in the HAZ on advancing side of the welds (Fig. 12). These observations are

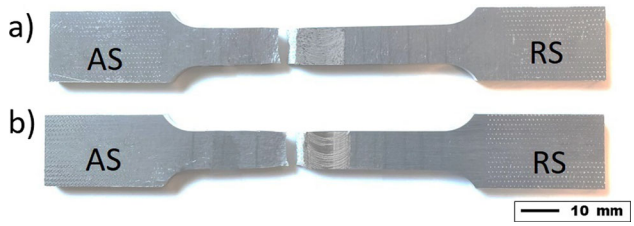

Fig. 12 Fracture locations of the welds produced with the tapered cylindrical pin (a) and the hexagonal pin with grooves (b)

consistent with the simulation studies and hardness observations. The lowest hardness was found in the HAZ on AS of the welds for both cases. Also, the larger HAZ was found on the AZ comparing to the HAZ on the RS of the welds. This is due to the increased heat input on the advancing side of the HAZ, as indicated by computer simulations, for both tool geometries. However, it should be noted that the results of computer simulations indicate that the highest thermal stresses of tensile nature, induced by the welding process, occur in the nugget zone. They are caused by the highest heat input in the mixing zone. However, recrystallization occurs in this zone, resulting in a reduction in grain size and re-precipitation. In the HAZ, due to sufficient heat input, the precipitates dissolute or overaging occurs, where enlargement and roughening of pre-existing particles can be observed, and no recrystallization process occurs (Ref 54). For precipitation hardened alloys like AA6082, the presence of the precipitates is crucial to provide desired mechanical properties. Consequently, in the case of a precipitation hardened alloy such as AA6082, in addition to thermal stresses, the presence of fine precipitates uniformly dispersed in the matrix material, as is the case in the nugget zone, also plays a key role in ensuring adequate mechanical properties. These observations are in a good agreement with the

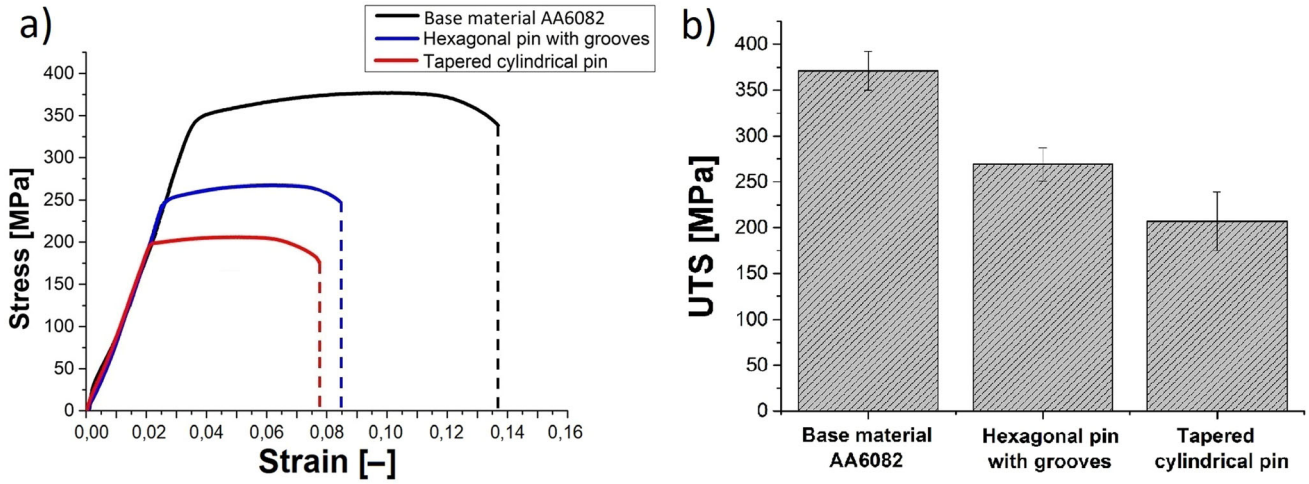

Fig. 13 Stress-strain curves for the produced FSW joints and the base material AA6082 (a) and their average UTS values (b)

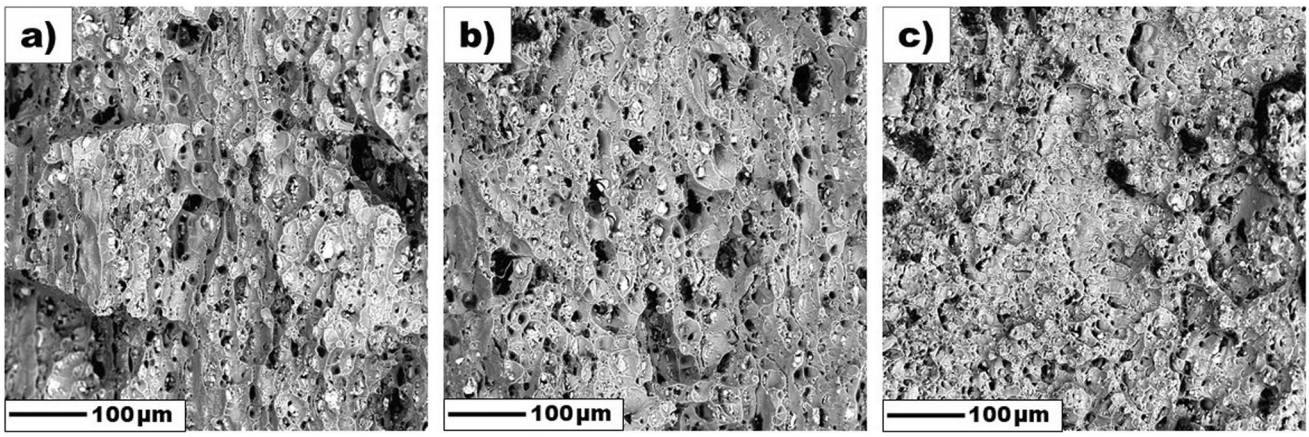

Fig. 14 Fracture surface of the base material AA6082 (a) and the FSW joints produced with the tapered cylindrical pin (b) and hexagonal pin with grooves (c) subjected to tensile tests

studies of Pabandi et al. (Ref 55) where two precipitation hardened alloys of AA6061 and AA2024 were friction stir welded. Regardless of the positioning of the alloys on AS or RS, the failure location after tensile tests was noted in HAZ. The failure location in the HAZ was also noted by Fathi et al. (Ref 56) for AA6061, Liu et al. (Ref 57) for AA2219, Patel et al. (Ref 58) for AA6063 and Rajendran et al. (Ref 59) for AA2014.

The fractography pictures of the FSW joints and the base material are presented in Fig. 14. As presented before, the fracture of the tested FSW tensile samples located in the HAZ region close to the original joint line on the advancing side. In the case of both welded samples, the fracture surface is quite homogenous. No significant surface irregularities can be observed, due to the fact that both samples ruptured out in the heat-affected zone, where no mixing occurred. It is notable that in the case of welds, the material cracked simultaneously in multiple parallel planes, and the individual cracks are connected together by perpendicular interplanar cracks. Fig. 14(b) and (c) clearly presents that the cracking proceeded in a ductile nature. The surface of the cracks consisted mainly of a large number of shallow and uniform dimples indicating mainly ductile behavior of the material. In the case of the base material (Fig. 14a), the dominant mechanism was ductile cracking with several brittle precipitates present, around which local voids were formed. The fracture surface of the base material consisting of long and flat areas corresponds to the elongated grains revealed by microstructural observations (Fig. 10a).

4. Conclusions

The present work focuses on simulation of Friction Stir Welding of AA6082 by applying two different tool geometries. This study also presents experimental results that provide microstructural observations and determination of the mechanical properties of the resulting welds. On the base of the experimental and simulation analysis the following conclusions can be determined:

1. Computer simulations revealed that when friction stir welding with the tool with a hexagonal pin with grooves

the maximum temperature is at least 5% higher than when welding with use of a tapered cylindrical pin with no grooves. During the welding simulations a maximum temperature of 406 ºC was noted for the welding with the complex pin. It was also noted that the temperature gradient is clearly higher in front of the tool than behind the tool.

2. The residual stresses introduced when using a simple pin are at least 13% lower than in the case of the complex pin. A higher maximum temperature at the weld centerline consequently increased the thermal residual stresses. The highest residual stresses introduced with the use of a complex pin reached about 237 MPa, while for the complex pin was equal to 210 MPa.
3. In the case of the complex pin, the maximum velocity of the material flow around the hexagonal region was at least 40% higher than the circular one, due to the higher heat generated around the hexagonal area, higher shear stresses, lower dynamic viscosity and as a result, higher flow rate. The presence of a slope in the simple pin affected the greater flow of the plasticized material.
4. In the produced welds, greater grain refinement was observed in the SZ as a result of applying the complex pin. In the case of the welds produced with the complex pin, the average grain size in the SZ was equal to 11 ± 1 μm, and in the case of the simple pin 14 ± 1 μm.
5. Hardness measurements revealed that the weld produced with the complex pin had a higher hardness in the SZ compared to the weld produced with the simple pin. The asymmetry of the hardness profile also indicates the existence of AS and RS.
6. Performed tensile tests revealed that the location of the lowest strength was the HAZ on the advancing side. The UTS of 269 ± 18 and 207 ± 32 MPa were noted for the joints produced with hexagonal pin with grooves and tapered cylindrical pin, respectively. It corresponded to the joint efficiency of 72.5 ± 4.9 and 55.8 ± 8.6 %.

Authors Contributions

All authors contributed to the study conception and design. Material preparation, data collection and analysis were performed by all authors. The first draft of the manuscript was written by AL, BS, BS, AT and PC and all authors commented on previous versions of the manuscript. All authors read and approved the final manuscript.

Funding

The authors declare that no funds, grants, or other support were received during the preparation of this manuscript.

Data availability

The datasets generated during and/or analyzed during the current study are available from the corresponding author on reasonable request.

Conflict of interest

The authors have no relevant financial or non-financial interests to disclose.

References

1. A. Laska and M. Szkodo, Manufacturing Parameters, Materials, and Welds Properties of Butt Friction Stir Welded Joints-Overview, *Materials (Basel)*, 2020, **13**, p 1–46
2. M. Mohammadi-pour, A. Khodabandeh, S. Mohammadi-pour, and M. Paidar, Microstructure and Mechanical Properties of Joints Welded by Friction-Stir Welding in Aluminum Alloy 7075–T6 Plates for Aerospace Application, *Rare Met.*, 2016 https://doi.org/10.1007/s12598-016-0692-9
3. A.R.S. Essa, M.M.Z. Ahmed, A.K.Y.A. Mohamed, and A.E. El-Nikhaily, An Analytical Model of Heat Generation for Eccentric Cylindrical Pin in Friction Stir Welding, *J. Mater. Res. Technol.*, 2016, **5**(3), p 234–240. https://doi.org/10.1016/j.jmrt.2015.11.009
4. M. Ilangovan, S. Rajendra Boopathy, and V. Balasubramanian, Effect of Tool Pin Profile on Microstructure and Tensile Properties of Friction Stir Welded Dissimilar AA 6061–AA 5086 Aluminium Alloy Joints, *Def. Technol.*, 2015, **11**(2), p 174–184. https://doi.org/10.1016/j.dt.2015.01.004
5. P. Cavaliere, Friction Stir Welding of Al Alloys: Analysis of Processing Parameters Affecting Mechanical Behavior, *Procedia CIRP*, 2013, **11**, p 139–144. https://doi.org/10.1016/j.procir.2013.07.039
6. A. Laska, M. Szkodo, Ł Pawłowski, and G. Gajowiec, Corrosion Properties of Dissimilar AA6082/AA6060 Friction Stir Welded Butt Joints in Different NaCl Concentrations, *Int. J. Precis. Eng. Manuf. Green Technol.*, 2022, **10**(2), p 457–477
7. A. Laska, M. Szkodo, P. Cavaliere, D. Moszczynska, and J. Mizera, Analysis of Residual Stresses and Dislocation Density of AA6082 Butt Welds Produced by Friction Sir Welding, *Metall. Mater. Trans. A*, 2022, **54**(1), p 211–225
8. S. Lim, S. Kim, C.G. Lee, and S. Kim, Tensile Behavior of Friction-Stri-Welded Al 6061-T651, *Metall. Mater. Trans. A Phys. Metall. Mater.*, 2004, **35 A**(9), p 2829–2835
9. A. Bandi and S.R. Bakshi, Effect of Pin Length and Rotation Speed on the Microstructure and Mechanical Properties of Friction Stir Welded Lap Joints of AZ31B-H24 Mg Alloy and AA6061-T6 Al Alloy, *Metall. Mater. Trans. A Phys. Metall. Mater. Sci.*, 2020, **51**(12), p 6269–6282. https://doi.org/10.1007/s11661-020-06020-8
10. A.H. Feng, D.L. Chen, and Z.Y. Ma, Microstructure and Cyclic Deformation Behavior of a Friction-Stir-Welded 7075 Al Alloy, *Metall. Mater. Trans. A Phys. Metall. Mater. Sci.*, 2010, **41**(4), p 957–971
11. A.H. Lotfi and S. Nourouzi, Effect of Welding Parameters on Microstructure, Thermal, and Mechanical Properties of Friction-Stir Welded Joints of Aa7075-T6 Aluminum Alloy, *Metall. Mater. Trans. A Phys. Metall. Mater. Sci.*, 2014, **45**(6), p 2792–2807
12. G. İpekoğlu, S. Erim, and G. Çam, Investigation into the Influence of Post-Weld Heat Treatment on the Friction Stir Welded AA6061 Al-

Alloy Plates with Different Temper Conditions, *Metall. Mater. Trans. A Phys. Metall. Mater. Sci.*, 2014, **45**(2), p 864–877
13. M. Abbasi, B. Bagheri, and F. Sharifi, Simulation and Experimental Study of Dynamic Recrystallization Process during Friction Stir Vibration Welding of Magnesium Alloys, *Trans. Nonferrous Met. Soc. China*, 2021, **31**(9), p 2626–2650. https://doi.org/10.1016/S1003-6326(21)65681-9
14. B. Bagheri, M. Abbasi, A. Abdolahzadeh, and A.H. Kokabi, Numerical Analysis of Cooling and Joining Speed Effects on Friction Stir Welding by Smoothed Particle Hydrodynamics (SPH), *Arch. Appl. Mech.*, 2020, **90**(10), p 2275–2296
15. B. Bagheri, A. Shamsipur, A. Abdollahzadeh, and S.E. Mirsalehi, Investigation of SiC Nanoparticle Size and Distribution Effects on Microstructure and Mechanical Properties of Al/SiC/Cu Composite during the FSSW Process: Experimental and Simulation, *Met. Mater. Int.*, 2023, **29**(4), p 1095–1112. https://doi.org/10.1007/s12540-022-01284-8
16. B. Bagheri, F. Sharifi, M. Abbasi, and A. Abdollahzadeh, On the Role of Input Welding Parameters on the Microstructure and Mechanical Properties of Al6061-T6 Alloy during the Friction Stir Welding: Experimental and Numerical Investigation, *Proc. Inst. Mech. Eng. Part L J. Mater. Des. Appl.*, 2022, **236**(2), p 299–318
17. T.U. Seidel and A.P. Reynolds, Visualization of the Material Flow in AA2195 Friction-Stir Welds Using a Marker Insert Technique, *Metall. Mater. Trans. A Phys. Metall. Mater. Sci.*, 2001, **32**(11), p 2879–2884
18. G.J. Bendzsak, T.H. North, and C.B. Smith, "An Experimentally Validated 3D Model for Friction Stir Welding," *Proceedings of the Second International Symposium of FSW, Gothenbutg*, 2000
19. P. Ulysse, Three-Dimensional Modeling of the Friction Stir-Welding Process, *Int. J. Mach. Tools Manuf.*, 2002, **42**(14), p 1549–1557
20. P.A. Colegrove and H.R. Shercliff, Experimental and Numerical Analysis of Aluminium Alloy 7075–T7351 Friction Stir Welds, *Sci. Technol. Weld. Join.*, 2003, **8**(5), p 360–368
21. P.A. Colegrove and H.R. Shercliff, 3-Dimensional CFD Modelling of Flow Round a Threaded Friction Stir Welding Tool Profile, *J. Mater. Process. Technol.*, 2005, **169**(2), p 320–327
22. R. Nandan, G.G. Roy, T.J. Lienert, and T. Debroy, Three-Dimensional Heat and Material Flow during Friction Stir Welding of Mild Steel, *Acta Mater.*, 2007, **55**(3), p 883–895
23. R. Nandan, G.G. Roy, T.J. Lienert, and T. Debroy, Numerical Modelling of 3D Plastic Flow and Heat Transfer during Friction Stir Welding of Stainless Steel, *Sci. Technol. Weld. Join.*, 2006, **11**(5), p 526–537
24. R. Nandan, G.G. Roy, and T. Debroy, Numerical Simulation of Three Dimensional Heat Transfer and Plastic Flow during Friction Stir Welding, *Metall. Mater. Trans. A Phys. Metall. Mater. Sci.*, 2006, **37**(4), p 1247–1259
25. D. Kim, H. Badarinarayan, J.H. Kim, C. Kim, K. Okamoto, R.H. Wagoner, and K. Chung, Numerical Simulation of Friction Stir Butt Welding Process for AA5083-H18 Sheets, *Eur. J. Mech. A/Solids*, 2010, **29**(2), p 204–215. https://doi.org/10.1016/j.euromechsol.2009.10.006
26. J.N. Reddy and D.K. Gartling, *The Finite Element Method in Heat Transfer and Fluid Dynamics*, CRC Press, Florida, 2010
27. A.F. Hasan, C.J. Bennett, P.H. Shipway, S. Cater, and J. Martin, A Numerical Methodology for Predicting Tool Wear in Friction Stir Welding, *J. Mater. Process. Technol.*, 2017, **241**, p 129–140. https://doi.org/10.1016/j.jmatprotec.2016.11.009
28. S.D. Ji, Q.Y. Shi, L.G. Zhang, A.L. Zou, S.S. Gao, and L.V. Zan, Numerical Simulation of Material Flow Behavior of Friction Stir Welding Influenced by Rotational Tool Geometry, *Comput. Mater. Sci.*, 2012, **63**, p 218–226
29. L. Zhang, S. Ji, G. Luan, C. Dong, and L. Fu, Friction Stir Welding of Al Alloy Thin Plate by Rotational Tool without Pin, *J. Mater. Sci. Technol.*, 2011, **27**(7), p 647–652
30. S. Hirasawa, H. Badarinarayan, K. Okamoto, T. Tomimura, and T. Kawanami, Analysis of Effect of Tool Geometry on Plastic Flow during Friction Stir Spot Welding Using Particle Method, *J. Mater. Process. Technol.*, 2010, **210**(11), p 1455–1463. https://doi.org/10.1016/j.jmatprotec.2010.04.003
31. Y. Zhenzhen, W. Zhang, H. Choo, and Z. Feng, Transient Heat and Material Flow Modeling of Friction Stir Processing of Magnesium Alloy Using Threaded Tool, *Metall. Mater. Trans. A Phys. Metall. Mater. Sci.*, 2012, **43**(2), p 724–737. https://doi.org/10.1007/s11661-011-0862-1
32. A. Laska, M. Szkodo, D. Koszelow, and P. Cavaliere, Effect of Processing Parameters on Strength and Corrosion Resistance of Friction Stir-Welded AA6082, *Metals (Basel)*, 2022, **12**(192), p 1–16
33. A.R. Darvazi and M. Iranmanesh, Prediction of Asymmetric Transient Temperature and Longitudinal Residual Stress in Friction Stir Welding of 304L Stainless Steel, *Mater. Des.*, 2014, **55**, p 812–820. https://doi.org/10.1016/j.matdes.2013.10.030
34. M.Z.H. Khandkar, J.A. Khan, A.P. Reynolds, and M.A. Sutton, Predicting Residual Thermal Stresses in Friction Stir Welded Metals, *J. Mater. Process. Technol.*, 2006, **174**(1–3), p 195–203
35. X.K. Zhu and Y.J. Chao, Numerical Simulation of Transient Temperature and Residual Stresses in Friction Stir Welding of 304L Stainless Steel, *J. Mater. Process. Technol.*, 2004, **146**(2), p 263–272
36. M.A. Waheed, L.O. Jayesimi, S.O. Ismail, and O.U. Dairo, Modeling of Heat Generations for Different Tool Profiles in Friction Stir Welding: Study of Tool Geometry and Contact Conditions, *J. Appl. Comput. Mech.*, 2017, **3**(1), p 37–59
37. Y. Zhu, G. Chen, Q. Chen, G. Zhang, and Q. Shi, Simulation of Material Plastic Flow Driven by Non-Uniform Friction Force during Friction Stir Welding and Related Defect Prediction, *Mater. Des.*, 2016, **108**, p 400–410. https://doi.org/10.1016/j.matdes.2016.06.119
38. G.Q. Chen, Q.Y. Shi, Y.J. Li, Y.J. Sun, Q.L. Dai, J.Y. Jia, Y.C. Zhu, and J.J. Wu, Computational Fluid Dynamics Studies on Heat Generation during Friction Stir Welding of Aluminum Alloy, *Comput. Mater. Sci.*, 2013, **79**, p 540–546. https://doi.org/10.1016/j.commatsci.2013.07.004
39. M.M. El-Sayed, A.Y. Shash, and M. Abd-Rabou, Finite Element Modeling of Aluminum Alloy AA5083-O Friction Stir Welding Process, *J. Mater. Process. Technol.*, 2017, **252**(September 2017), p 13–24. https://doi.org/10.1016/j.jmatprotec.2017.09.008
40. B. Sadeghian, A. Taherizadeh, M. Atapour, N. Saeidi, and A. Alhaji, Phase-Field Simulation of Microstructure Evolution during Friction Stir Welding of 304 Stainless Steel, *Mech. Mater.*, 2021, **163**(July), p 104076. https://doi.org/10.1016/j.mechmat.2021.104076
41. B. Sadeghian, A. Taherizadeh, and M. Atapour, Simulation of Weld Morphology during Friction Stir Welding of Aluminum- Stainless Steel Joint, *J. Mater. Process. Technol.*, 2018, **259**(February), p 96–108. https://doi.org/10.1016/j.jmatprotec.2018.04.012
42. M. Riahi and H. Nazari, Analysis of Transient Temperature and Residual Thermal Stresses in Friction Stir Welding of Aluminum Alloy 6061–T6 via Numerical Simulation, *Int. J. Adv. Manuf. Technol.*, 2011, **55**(1–4), p 143–152
43. P. Poolperm, W. Nakkiew, and N. Naksuk, Finite Element Analysis of the Effect of Porosity on Residual Stress in 2024 Aluminium Alloy GTAW, *Mater. Res. Express*, 2020, **7**(5), p 56518. https://doi.org/10.1088/2053-1591/ab906a
44. M. Abbasi, B. Bagheri, A. Abdollahzadeh, and A.O. Moghaddam, A Different Attempt to Improve the Formability of Aluminum Tailor Welded Blanks (TWB) Produced by the FSW, *Int. J. Mater. Form.*, 2021, **14**(5), p 1189–1208
45. M. Abbasi, A. Abdollahzadeh, B. Bagheri, A. Ostovari Moghaddam, F. Sharifi, and M. Dadaei, Study on the Effect of the Welding Environment on the Dynamic Recrystallization Phenomenon and Residual Stresses during the Friction Stir Welding Process of Aluminum Alloy, *Proc. Inst. Mech. Eng. Part L J. Mater. Des. Appl.*, 2021, **235**(8), p 1809–1826
46. S.N. Naik and S.M. Walley, The Hall-Petch and Inverse Hall-Petch Relations and the Hardness of Nanocrystalline Metals, *J. Mater. Sci.*, 2020, **55**(7), p 2661–2681. https://doi.org/10.1007/s10853-019-04160-w
47. K. Surekha and A. Els-Botes, Development of High Strength, High Conductivity Copper by Friction Stir Processing, *Mater. Des.*, 2011, **32**(2), p 911–916. https://doi.org/10.1016/j.matdes.2010.08.028
48. P.L. Threadgill, A.J. Leonard, and H. Shercliff, Friction Stir Welding of Aluminium Alloys, *Int. Mater. Rev.*, 2009, **54**(2), p 49–93
49. L.-E. Svensson, L. Karlsson, H. Larsson, B. Karlsson, M. Fazzini, and J. Karlsson, Microstructure and Mechanical Properties of Friction Stir Welded Aluminium Alloys with Special Reference to AA 5083 and AA 6082, *Sci. Technol. Weld. Join.*, 2000, **5**(5), p 285–296. https://doi.org/10.1179/136217100101538335
50. Z. Zhang, B.L. Xiao, and Z.Y. Ma, Effect of Welding Parameters on Microstructure and Mechanical Properties of Friction Stir Welded 2219Al-T6 Joints, *J. Mater. Sci.*, 2012, **47**(9), p 4075–4086

51. R. Kosturek, J. Torzewski, M. Wachowski, and L. Śnieżek, Effect of Welding Parameters on Mechanical Properties and Microstructure of Friction Stir Welded AA7075-T651 Aluminum Alloy Butt Joints, *Materials (Basel)*, 2022, **15**(5950), p 1–15
52. W. Wang, S. Zhang, K. Qiao, K. Wang, P. Peng, S. Yuan, S. Chen, T. Zhang, Q. Wang, T. Liu, and Q. Yang, Microstructure and Mechanical Properties of Friction Stir Welded Joint of TRIP Steel, *J. Manuf. Process.*, 2020, **56**(13), p 623–634. https://doi.org/10.1016/j.jmapro.2020.05.045
53. N.K. Babu, K. Kallip, M. Leparoux, K.A. AlOgab, X. Maeder, and Y.A.R. Dasilva, Influence of Microstructure and Strengthening Mechanism of AlMg5-Al2O3 Nanocomposites Prepared via Spark Plasma Sintering, *Mater. Des.*, 2016, **95**, p 534–544. https://doi.org/10.1016/j.matdes.2016.01.138
54. M.M. Krishnan, Overview of the Effect of Post Welded Heat Treatment on Friction Stir Welding Of Aluminum Alloys, *Int. J. Eng. Innov. Technol.*, 2013, **2**(9), p 76–80
55. H.K. Pabandi, H.R. Jashnani, and M. Paidar, Effect of Precipitation Hardening Heat Treatment on Mechanical and Microstructure Features of Dissimilar Friction Stir Welded AA2024-T6 and AA6061-T6 Alloys, *J. Manuf. Process.*, 2017, **31**, p 214–220. https://doi.org/10.1016/j.jmapro.2017.11.019
56. J. Fathi, P. Ebrahimzadeh, R. Farasati, and R. Teimouri, Friction Stir Welding of Aluminum 6061–T6 in Presence of Watercooling: Analyzing Mechanical Properties and Residual Stress Distribution, *Int. J. Light. Mater. Manuf.*, 2019, **2**(2), p 107–115. https://doi.org/10.1016/j.ijlmm.2019.04.007
57. H.J. Liu, H.J. Zhang, Y.X. Huang, and L. Yu, Mechanical Properties of Underwater Friction Stir Welded 2219 Aluminum Alloy, *Trans. Nonferrous Met. Soc. China (English Ed., The Nonferrous Metals Society of China)*, 2010, **20**(8), p 1387–1391. https://doi.org/10.1016/S1003-6326(09)60309-5
58. V. Patel, J. De Backer, H. Hindsefelt, M. Igestrand, S. Azimi, J. Andersson, and J. Säll, High Speed Friction Stir Welding of AA6063-T6 Alloy in Lightweight Battery Trays for EV Industry: Influence of Tool Rotation Speeds, *Mater. Lett.*, 2022, **318**, p 132135
59. C. Rajendran, G. Parthiban, K. Pranav, and S.P. Nithi Balaji, Influence of Solution Treatment and Artificial Aging OnFracture Load of Friction Stir Welded Lap Joints of AA2014-T6, *IOP Conf. Ser. Mater. Sci. Eng.*, 2021, **1059**(1), p 012037